X-ray Source Population Studies of Cen A (NGC 5128) with Chandra Data

Bachelorarbeit aus der Physik

Vorgelegt von

Katharina Egg

22.05.2020

Dr. Karl Remeis-Sternwarte
Friedrich-Alexander-Universität Erlangen-Nürnberg

Betreuerin: Prof. Dr. Manami Sasaki

Abstract

In the course of this thesis X-ray data of the galaxy Centaurus A (Cen A, NGC 5128) taken by the Chandra X-ray Observatory were analyzed.
After some general information about Centaurus A, the Chandra X-ray Observatory, and possible sources, the process and results of the analysis shall be presented.
Using the data of all available ACIS Chandra observations taken between December 10th, 1999 and April 24th, 2019, 418 X-ray point sources could be detected. For 396 sources counts were extracted and hardness ratios calculated. The X-ray source list was then cross-correlated against optical, infrared, and radio catalogs. The resulting magnitudes, hardness ratios, and counts were plotted and allowed some conclusions as to the nature of the sources in the field of Cen A. Five foreground stars could be identified, as well as a number of foreground star candidates. Background sources were found as well, as were radio sources, two of which qualify as supernova remnant (SNR) candidates. Lastly, theoretical isochrones for stars in our Milky Way and in Cen A were plotted into an optical color-magnitude diagram. Between the isochrones and the data a correlation could be observed.
Further analysis of the temporal variability and spectra remains to be conducted and will be carried out in the future.

Table of Contents

List of Figures

1. Introduction

Compared to the age of astronomy as a whole, X-ray astronomy is still a fairly young discipline. Observing anything at all at X-ray wavelengths used to be a distant dream, as astronomical observations used to be strictly limited to optical light and optical light alone.

The reason for this lies in the nature of earth's atmosphere. Figure 1.1 illustrates the transmission of light of different wavelengths through earth's atmosphere. It becomes clear that the fact that our eyes are attuned to visible light is no coincidence. Visible light occupies a very narrow region on the spectrum of electromagnetic radiation, where light is able to pass through earth's atmosphere almost unhindered. Most higher energetic radiation, however, is absorbed. In our daily life this is quite fortunate, as prolonged exposure to X-rays or γ-rays would be exceedingly detrimental to our health. For observations of X-ray sources, however, this means that the detection will have to occur at very high altitudes (Seward and Charles, 2010).

As can be seen in Figure 1.1, the observations of quite highly energetic X-rays might still be possible with a balloon, for X-rays of a lower energy, however, a rocket or, even better, a satellite is needed. This proved quite the challenge for the astronomers and engineers of the 1950s and 1960s, who had the task of inventing detectors, not only small enough to put on rockets and satellites, but also robust and self-sufficient enough to withstand the harsh conditions of space and continue functioning over a long period of time without any maintenance (Seward and Charles, 2010).

These ventures were not always successful, a rocket launch in October 1961, for instance, worked very well, only for the team to discover afterwards that the doors in front of the detector would not open. In its successor, however, this weakness was eliminated and it went on to observe the first X-ray source aside from the sun, Sco-X1 (Seward and Charles, 2010).

Since then a lot of progress has been made. Several X-ray satellites, e.g. Uhuru, helped identify a great number of X-ray sources, until the first all-sky survey was conducted with ROSAT in the 1990s (Seward and Charles, 2010).
The resolution of the instrumentation increased over time. In 1989 the Einstein Satellite was able to detect individual X-ray sources in nearby galaxies for the first time due to its - at the time - unprecedented resolution (Fabbiano, 2006).

The Chandra X-ray Observatory, that was launched in 1999 and the data of which will be analyzed in the course of this thesis, has a higher resolution still, enabling us to conduct

source population studies in other, more distant galaxies (Garmire et al., 2003).

Such a population study - although of a galaxy not too far from us - will also be the subject of this thesis. Using Chandra data taken over the course of almost 20 years, the nature of the sources in the galaxy Centaurus A will be examined.

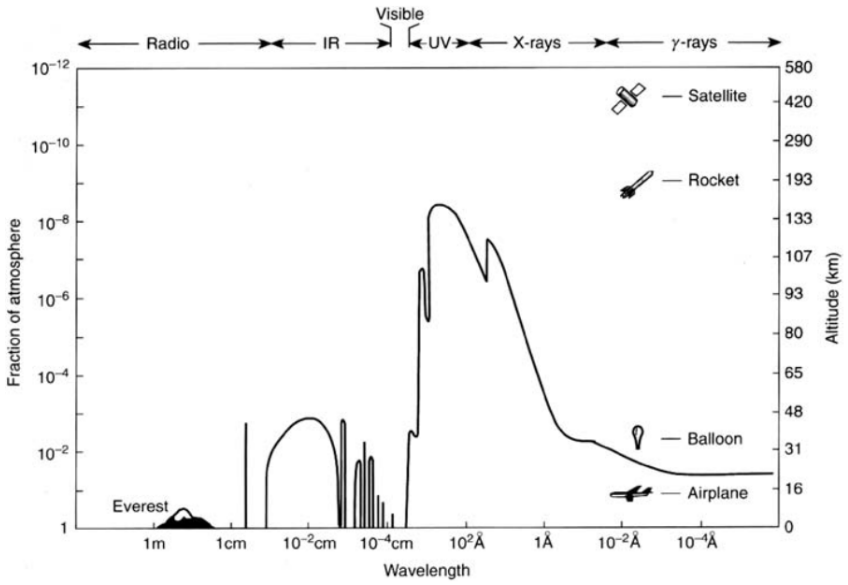

Figure 1.1.: Transmission of electromagnetic light through earth's atmosphere per wavelength; the solid line indicates the altitude where half of the radiation is absorbed (Seward and Charles, 2010)

2. Centaurus A, the Chandra X-ray Observatory, and X-ray Sources

Before the analysis of Chandra data is presented, some general information on Cen A, the Chandra X-ray Observatory, and X-ray sources, that will be studied, will be given in this chapter.

2.1. Centaurus A

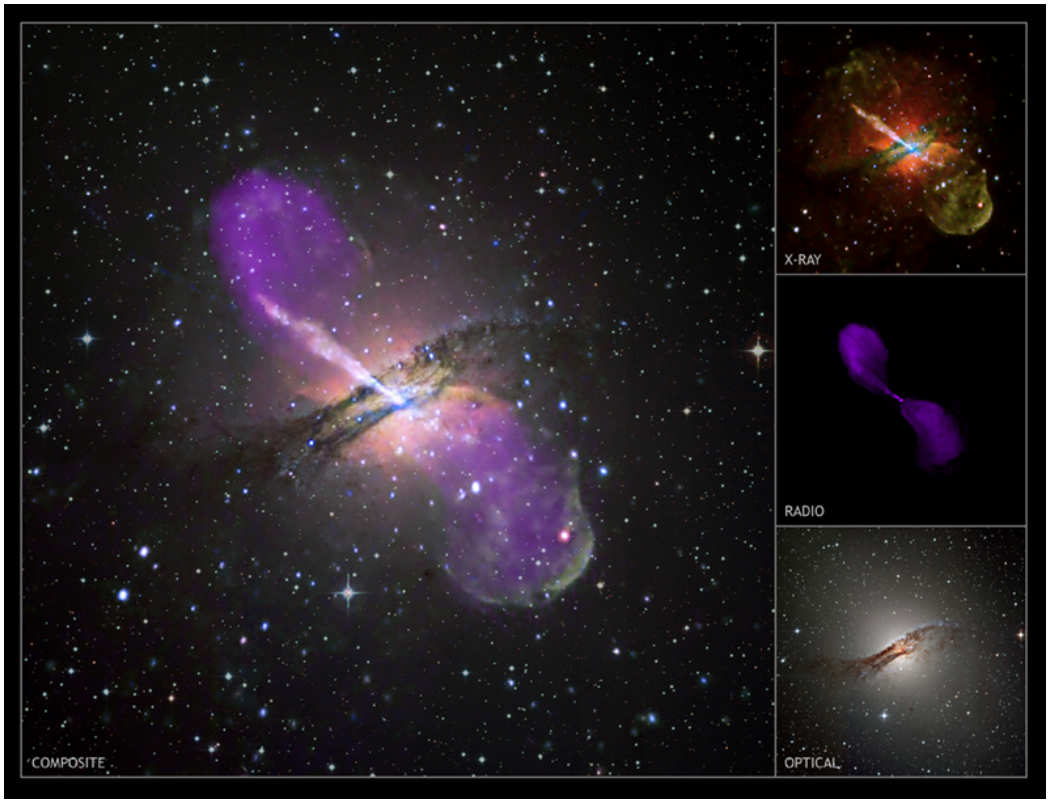

Figure 2.1.: Different wavelength images of Cen A taken with Chandra, the VLA, and the VLT, as well as a composite image (HEASARC, 2012)

Centaurus A (Cen A), also known as NGC 5128, is our nearest X-ray and radio-emitting active galaxy. Due to its close proximity to us it is a great target to study these mechanisms in detail. It emits a lot of interesting features across the electromagnetic spectrum, as can

be seen in Figure 2.1. It has been classified as a Fanaroff–Riley type I galaxy according to the classification system devised by Fanaroff and Riley (1974) (McKinley et al., 2018). This refers to the brightest radio emission regions of Cen A being located at the center instead of being extended across the galaxy (Fanaroff and Riley, 1974).

The mass of the supermassive black hole at the center of Cen A has been measured to $M_{\mathrm{BH}} = 4.5(+1.7, -1.0) \times 10^7\, M_\odot$ and $M_{\mathrm{BH}} = (5.53.0) \times 10^7\, M_\odot$ using H_2 kinematics and stellar kinematics respectively (Neumayer, 2010). Cen A is also in agreement with the $M_{\mathrm{BH}} - \sigma$ relation between the masses of supermassive black holes and the velocity dispersions of their host galaxy's bulges (Merritt and Ferrarese, 2001).

Cen A is located in the southern hemisphere (RA = 13 25 27.6, Dec = -43 01 08.8, courtesy of the SIMBAD database, http://simbad.u-strasbg.fr/simbad/) in the Centaurus constellation. Using five independent methods, the median of its distance to us could be determined to be 3.8 Mpc by Harris et al. (2010).

The first one to take note of Cen A's interesting structure was Herschel in the 19th century. It once again became an object of interest for its radio activity at the dawn of radio astronomy in the 1950s (Israel, 1998). The radio source Cen A, along with several others, was found by Bolton (1948) and discovered to coincide with the galaxy NGC 5128 by Bolton et al. (1949).
In recent years the big radio lobes of Cen A (as can be seen in Figure 2.1) have been studied in great detail in order to find out more about AGN activity and its influence on the galaxy, the star formation within it, and the surrounding medium. A few interesting discoveries have been made, the uniformity of the outer lobes, for instance, implies the existence of not only a continuous energy supply from the AGN but also some in situ excitation mechanism. The southern radio lobe seems to be slightly disconnected from the center of the galaxy. As the southern lobe seems to be still continuously supplied with energy, this leads to the theory that there is simply not enough H I gas in this area to show any radio emission (McKinley et al., 2018).

In the optical, as can be seen in Figure 2.1, the image is dominated by a dust lane - approximately perpendicular to the radio lobes. This peculiar shape - an elliptical galaxy, split in two by a dust lane of spiral shape - has given rise to the theory that Cen A is the result of a galaxy merger between two such galaxies (Seward and Charles, 2010).

As a source of X-ray radiation Cen A was first detected by Bowyer et al. (1970). Its shape in the X-ray is not entirely unlike its appearance at radio wavelengths, as can be seen in Figure 2.1, as the X-ray jets align with the radio lobes and thus provide more insight into the workings of the AGN. The southern jet is, again, fainter than its northern counterpart (Seward and Charles, 2010), similar to what can be observed at mid-range distances at radio wavelengths.
The active galactic nucleus of Cen A is bright in the X-ray (as can be seen in Figure 2.1),

however, AGN effects are not the only aspect of this galaxy that can be studied at X-ray wavelengths. Cen A is one of our nearest neighboring galaxies, near enough that it can be resolved into individual stars, so its stellar population can be studied. Voss and Gilfanov (2006) found 272 X-ray point sources, approximately half of which are thought to be low mass X-ray binaries (LMXBs). Woodley et al. (2008) detected 353 X-ray point sources and found that a significant portion of the LMXB population occurs within globular clusters. In the course of this thesis, too, such a population study of Cen A will be undertaken.

In any case, Cen A, being a fascinating object at a quite short distance, is a great opportunity to study the characteristics of a galaxy on a large scale, be it the effects of its active center or its population.

2.2. The Chandra X-ray Observatory

The Chandra X-ray Observatory - initially called Advanced X-ray Astrophysics Facility (AXAF) - was launched on July 23, 1999 (Brissenden, 2001). The Chandra satellite is large, it possesses a wing span of 19.5 m, a length (with open sun-shade door) of 11.8 m, and a weight of 4800 kg (Brissenden, 2001).

Figure 2.2 shows the process of Chandra collecting X-rays. It can be seen that an array of mirrors focuses the X-rays onto an instrument in the back. In Figure 2.3 these mirrors can be seen in more detail and it becomes clear that the mirror array is almost parallel to the infalling X-rays. This is due to the fact that X-rays will only reflect at small grazing angles (Schwartz, 2011).

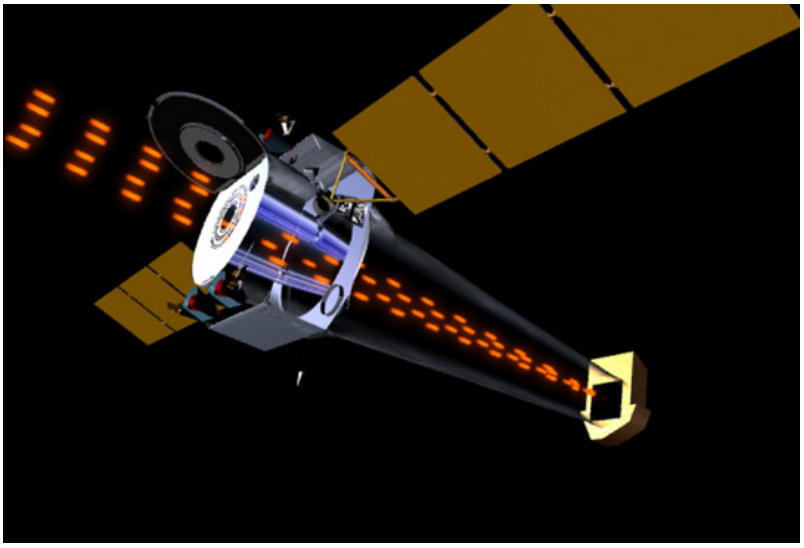

Figure 2.2.: Schematic of Chandra collecting light (Chandra X-Ray Observatory, 2009c)

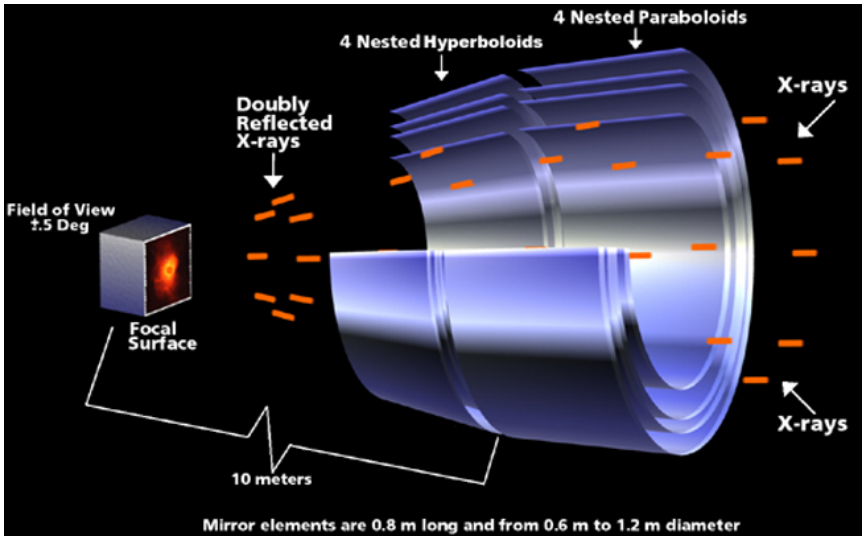

Figure 2.3.: Schematic of Chandra's mirrors (Chandra X-Ray Observatory, 2009c)

Each mirror possesses two components, a parabolic and a hyperbolic mirror, reflecting the light twice, before it can reach the CCD array. A parabolic mirror will reflect light that is parallel to its axis towards its focal point. However, slight divergences in the incident angle of the light will simply cause a linear increase in the size of the image but still contribute to the on-axis target. So any X-Ray source in Chandra's field of view would contribute, which is not an effect that is wanted here. This is why a second, hyperbolic mirror is needed (Schwartz, 2011).

This mirror configuration, comprised of a parabolic and a hyperbolic mirror, is called a Wolter I Type mirror and is used in many X-Ray telescopes. It ensures that angular distance to the on-axis target will translate linearly into distance on the focal plane. The effective area of the mirror configuration depends on the grazing angles (25" to 55" for Chandra), so several mirrors are used in a nested configuration to increase the effective area (Schwartz, 2011).

The X-ray photons can now be focused on either the Advanced CCD Imaging Spectrometer (ACIS) or the High Resolution Camera (HRC). As to their respective spectroscopy arrays, the former is optimized for high energy X-rays, the latter for lower energy X-rays (Brissenden, 2001). Their imaging arrays differ in term of resolution. The ACIS has a higher energy resolution, while the HRC has a larger field of view (Chandra X-Ray Observatory, 2009a,b). In the course of this thesis only ACIS data were used. ACIS data span an energy range from 0.5 to 7 keV (Chandra X-Ray Observatory, 2019). Chandra also contains two movable gratings, the High Energy Transmission Grating (HETG) and the Low Energy Transmission Grating (LETG), that can be used to produce a spectrum on one of the spectroscopic detectors (Brissenden, 2001).

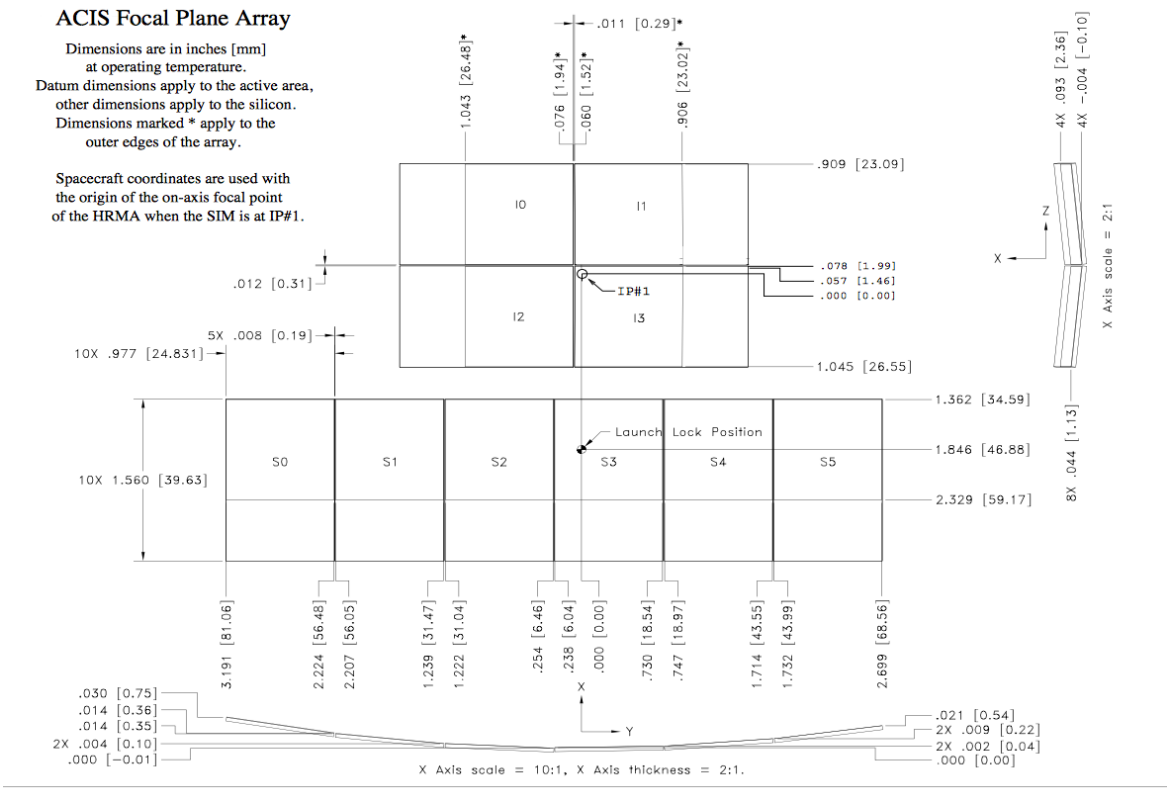

Figure 2.4.: Schematic of Chandra's ACIS array (Garmire et al., 2003)

The setup of the ACIS array can be seen in Figure 2.4. It consists of a 2×2 array for imaging, dubbed ACIS-I, and a 1×6 spectroscopic array, dubbed ACIS-S. Each CCD is of 1024×1024 format with 24 μm pixel size (Brissenden, 2001).

The amount of data produced by this setup is quite high, so certain operations, for example the elimination of cosmic ray events, are conducted on board, before the data are sent to the ground station (Garmire et al., 2003).

The high angular resolution of the ACIS arrays, which is better than 0.5 arc seconds on-axis, makes the study of individual extragalactic X-ray sources possible (Garmire et al., 2003).

2.3. X-ray Sources

The ultimate goal of this analysis is to find and study the X-ray sources in Centaurus A. Foreground and background sources will be eliminated and other objects, e.g. X-ray binaries and supernova remnants, will be identified.

In the following, a short overview over the objects that will be encountered in the analysis of X-ray data will be given. After a description as to the nature of the object, I will briefly outline how this particular object can be identified in the later analysis.

2.3.1. Foreground Stars

Foreground stars are objects that do not belong to Centaurus A at all. Instead, these stars are part of the Milky Way and just happen to be in the same field of view as Centaurus A. As such, these are sources we will be looking to identify and then eliminate from further analysis.

Foreground stars can be identified through their high magnitudes in the soft X-ray bands, compared to harder bands. Their optical and infrared counterparts are very bright, the flux of their optical counterparts is higher than their X-ray flux (Maccacaro et al., 1988; Saeedi et al., 2019).

2.3.2. Background Sources (Galaxies and Active Galactic Nuclei)

Background sources are, so to speak, the opposite of the foreground stars described in section 2.3.1. They are galaxies and active galactic nuclei (AGNs) that happen to be in the background of Centaurus A, but still contribute X-ray flux. They, too, are sources we will try to eliminate from further analysis.

Background sources can be found by looking at their counterparts in the infrared (Salvato et al., 2018). Especially sources with a radio counterpart may be AGN candidates (Pietsch, 2008).

2.3.3. Supernova Remnants

Supernova remnants (SNRs) are the remnants of stars that have blown up in a supernova explosion. Generally, the most common types of supernovae are type Ia and type II supernovae.

Type Ia supernovae are thought to occur in white dwarfs, which are the evolutionary endpoints of stars of approximately solar mass. A supernova occurs in an initially stable white dwarf if its mass exceeds the Chandrasekhar limit of $1.4\,M_\odot$ due to it accreting mass from another source, e.g. a binary partner. Once that happens, the electron degeneracy pressure is not strong enough to stop the white dwarf from collapsing further. Its core temperature rises, fusing oxygen and carbon, which causes an explosive wave, that rips the white dwarf apart. The shape of the resulting lightcurves is quite distinct, which even makes the determination of the distance of supernovae of this type possible. A well known type Ia supernova is Tycho's supernova (Seward and Charles, 2010).

Type II supernovae, on the other hand, occur at the end of the lives of stars with a much higher mass (more than approximately 10 solar masses). Once the hydrogen in their core has been depleted, the star contracts, which raises the temperature of the stellar core, allowing the fusion process to continue, producing ever heavier elements until it comes to a standstill at iron, the endpoint of the fusion process. At this point, the iron core is surrounded by layers of lighter elements, produced by the ongoing fusion in the outer layers of the star. The iron core is kept stable by electron degeneracy pressure, but as the pressure and the temperature grow, the iron of the core starts to decompose, first into lighter elements, then into protons and electrons, which finally combine to form neutrons. As electrons start to disappear, the core will collapse in a matter of seconds, causing a major shockwave, that catapults the outer layers of the star far into space. Left of the core is now only a neutron star (even heavier stars may even evolve into a black hole). A well known type II supernova is SN1987A (Seward and Charles, 2010).

Several mechanisms can produce X-rays in supernova remnants, many of which stem from the early stages of the remnant or the supernova explosion itself. An emerging neutron star at the center of the remnant can also contribute to the X-ray flux. Most of the X-ray emission of older SNRs is caused by the heating of the ejected outer layers of the star, as they collide with other material (Seward and Charles, 2010).

SNRs can be identified by their soft X-ray flux, combined with the fact that they possess a radio counterpart. The radio emission, which is non-thermal in nature, is caused by the compression of magnetic fields in the collisionless shock of the supernova (Seward and Charles, 2010).
The individual spectrum also plays a big role in the identification of an SNR. The spectral analysis could not be performed in the scope of this thesis, but will be carried out at a future date.

2.3.4. X-ray Binaries

X-ray Binaries (XRBs) are binary stars, that can be observed at X-ray wavelengths. The binary system consists of a regular star and a compact object, which can be a neutron star or a black hole. A binary system with a white dwarf as the compact object, meanwhile, is called a cataclysmic variable. The basic mechanism of the binary system does actually not vary too much for different compact objects. The energy, that is released in the form of X-ray radiation, is generated through gravitation, as mass from the star is accreted onto the compact object (Seward and Charles, 2010).

There are two basic forms of X-ray binaries, one distinguishes between High Mass X-ray binaries (HMXBs) and Low Mass X-ray binaries (LMXBs), referring to the mass of the regular star in the system. An artist's conception of their different configurations can be seen in Figure 2.5 (Seward and Charles, 2010).

The star in an HMXB will be very massive and bright, possessing powerful stellar winds. Through these stellar winds mass is accreted onto the compact object. This process can be seen in Figure 2.5. At optical wavelengths only the star will be detectable (Seward and Charles, 2010).
LMXBs, on the other hand, contain a star of a quite low mass, that does not possess strong stellar winds. The star fills its Roche lobe (the surface of equal gravity) and transfers mass onto the compact object through the inner Lagrangian point. For the system to be stable, the star's mass needs to be lower than the compact object's mass. For an average neutron star binary, for instance, this would mean that the mass of the star needs to be smaller than about $1.4\,M_{\odot}$ (the average mass of a neutron star). The optical counterparts of LMXBs are consequently very hard and sometimes impossible to detect (Seward and Charles, 2010).

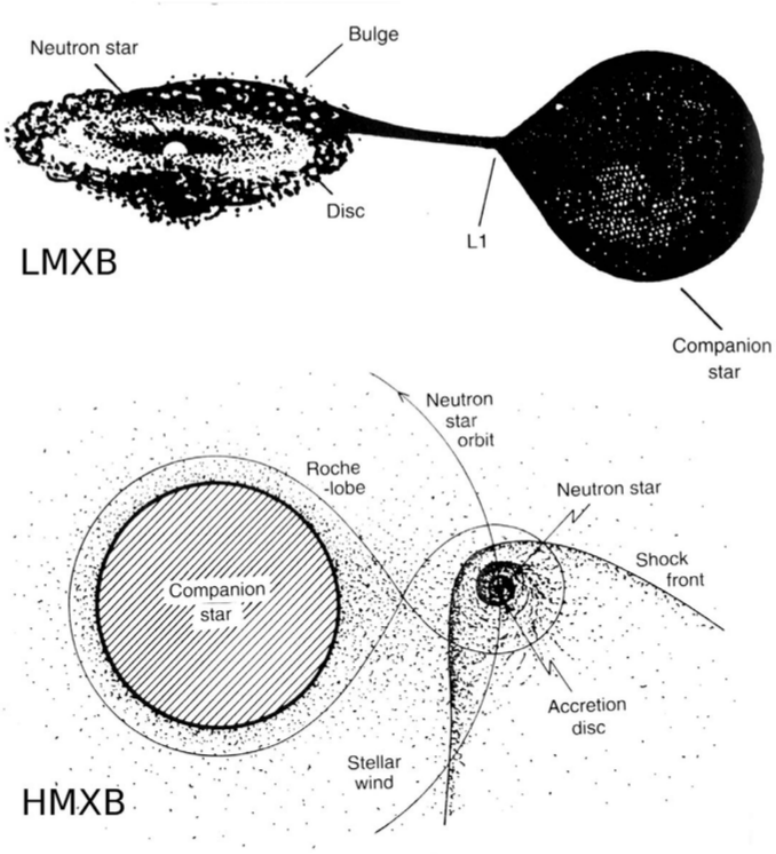

Figure 2.5.: Artist's conception of LMXBs and HMXBs (Seward and Charles, 2010)

X-Ray binaries can be identified through their variability (Pietsch, 2008). As the variability was not analyzed in the course of this thesis, the identifcation of X-ray binaries was not possible. However, as foreground and background sources were found, the remaining, as of yet unidentified sources should include the X-ray binaries of Cen A. Further analysis of these sources and their variabilities will be conducted in the future.

3. Analysis of Chandra Data and Results

The data analyzed in the course of this bachelor's thesis consist of all ACIS (Advanced CCD Imaging Spectrometer) observations taken with Chandra between December 10th, 1999 and April 24th, 2019. The full list of observation IDs can be found in the Appendix (A.1, p. 32).

3.1. Reprocessing of Data and Region Sorting

The data were reprocessed using the Chandra CIAO reprocessing script. This process ensures that the calibration of the data is up to date and as accurate as possible.

A destreaking of the data as well as the source detection and extraction of the X-ray point source regions was carried out by Tathagata Saha and Alex Markowitz from the Nicolaus Copernicus Astronomical Center in Warsaw. A broadband and an RGB image of the destreaked and stacked data can be seen in Figure 3.1 and Figure 3.2 respectively.
Afterwards they were manually checked for authenticity of the detected sources. A few initially overlooked sources were also added manually. For this process the data were analyzed using the program SAOImageDS9 in the ACIS Source Detection Energy Bands (Table 3.1).

Name	Energy Range [keV]
soft	0.5 - 1.2
medium	1.2 - 2.0
hard	2.0 - 7.0

Table 3.1.: ACIS Source Detection Energy Bands (Chandra X-Ray Observatory, 2019)

All detected X-ray sources can be seen in Figure 3.3. The colors of the regions in Figure 3.3 indicate the flags denoted in Table 3.2. All sources that are part of the jet were not further analyzed in the course of this thesis.

region color	meaning
blue	valid X-ray source
red	something the program mistakenly flagged as a source
white	valid X-ray source that the program missed and I added manually
yellow	part of the jet

Table 3.2.: Meaning of region colors in Figure 3.3

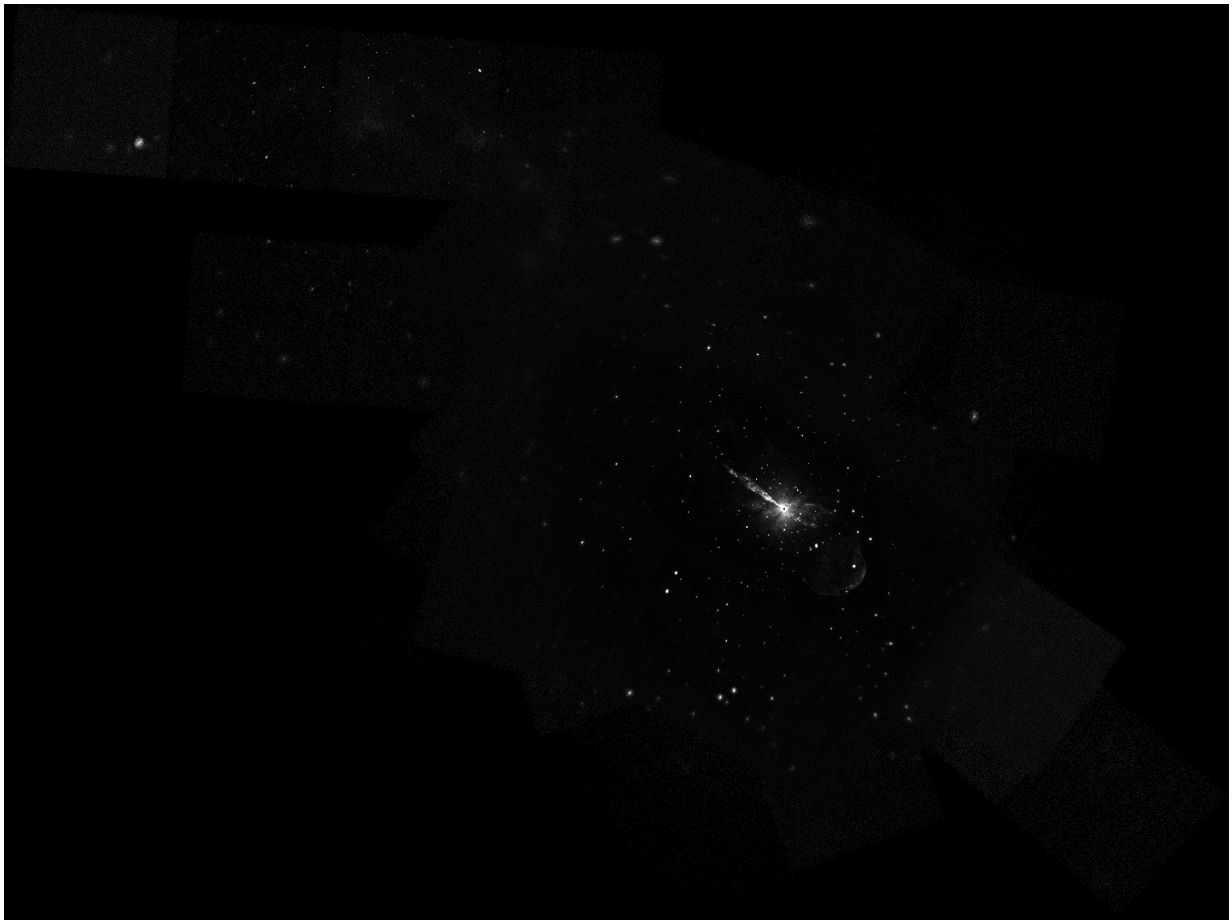

Figure 3.1.: Broadband image of destreaked and stacked Chandra data

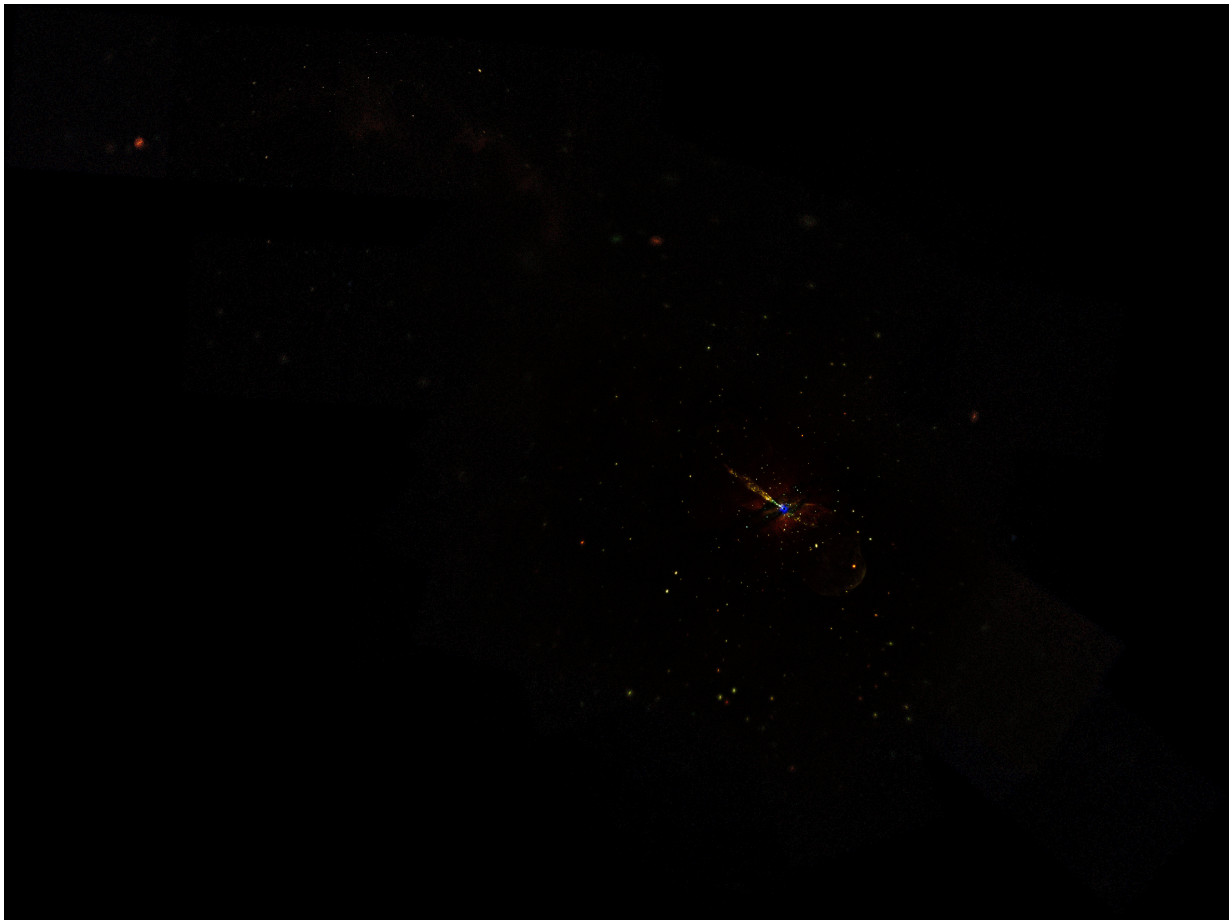

Figure 3.2.: RGB image of destreaked and stacked Chandra data (bands in accordance with Table 3.1)

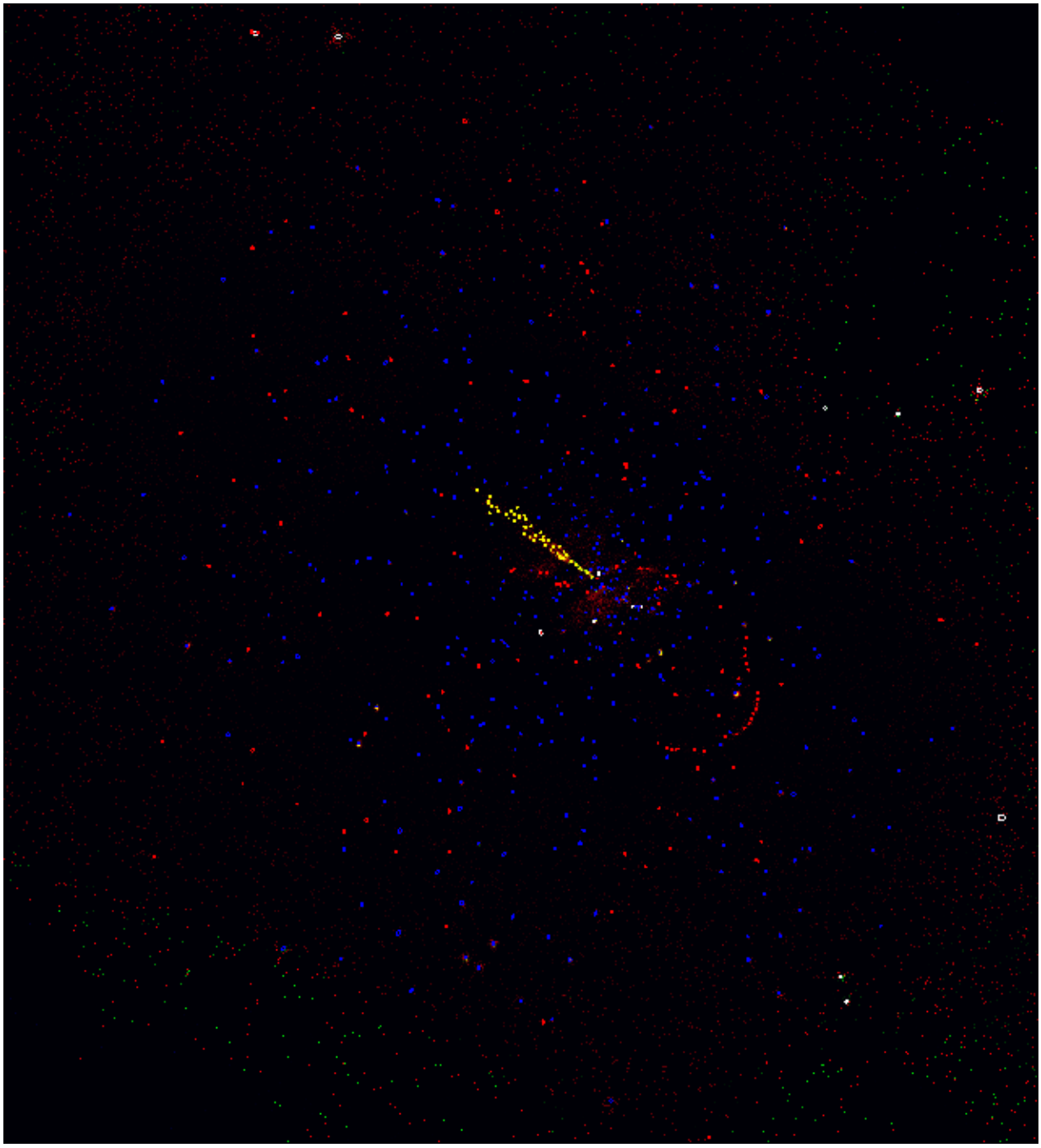

Figure 3.3.: X-ray source regions in Cen A

3.2. Hardness Ratios and Counts

The spectra of all X-ray sources were extracted by Prof. Dr. Jörn Wilms (Dr. Karl Remeis-Observatory Bamberg).
As a next step, the counts for each source and band, i.e. the number of photons to be detected from a source in a certain energy range, were calculated. Using these values, hardness ratios (HRs) were calculated. Hardness ratios are a good tool to compare the X-ray activity of sources in different bands against one another, as one hardness ratio value already encompasses information on two bands.

To calculate the counts and hardness ratios, I wrote a script in the language isis. It accessed each spectrum and summed over the counts of the bins corresponding to each ACIS Science band. The energy ranges of the ACIS Science bands can be seen in Table 3.3.

The error for the count of each band was calculated as follows:

$$ER = \sqrt{\sum_{\text{low}<\text{i}\leq\text{high}} ER_{\text{i}}^2} \tag{3.2.1}$$

With ER denoting the error of the whole band, ER_{i} denotes the error of each individual bin. Low and high denote the lower and upper limit of the energy band respectively.

Hardness Ratios of the type $(H\text{-}S)/(H+S)$ (H denoting the harder band and S the softer one) were calculated in accordance with Sasaki et al. (2018), using counts instead of count rates. Thus the following equation was used (Sasaki et al., 2018):

$$HR_{\text{i}} = \frac{B_{\text{i}+1} - B_{\text{i}}}{B_{\text{i}+1} + B_{\text{i}}} \tag{3.2.2}$$

The subsequent error for each hardness ratio was calculated as follows (Sasaki et al., 2018):

$$EHR_{\text{i}} = 2\frac{\sqrt{(B_{\text{i}+1}\,EB_{\text{i}})^2 + (B_{\text{i}}\,EB_{\text{i}+1})^2}}{(B_{\text{i}+1} + B_{\text{i}})^2} \tag{3.2.3}$$

In these equations B_{i} denotes the counts and EB_{i} the error of the counts of the band numbered i. The four bands of Chandra thus correspond to three hardness ratios.

Name	Energy Range [keV]
ultrasoft	0.2 - 0.5
soft	0.5 - 1.2
medium	1.2 - 2.0
hard	2.0 - 7.0

Table 3.3.: ACIS Science Energy Bands (Chandra X-Ray Observatory, 2019)

A second set of hardness ratios of the type $(H\text{-}S)/F$ was calculated using the following equation:

$$CHR_{\mathrm{i}} = \frac{B_{\mathrm{i+1}} - B_{\mathrm{i}}}{F} \tag{3.2.4}$$

Here F denotes the total counts, i.e. the sum over the counts of all bands for each respective source.

The error for each hardness ratio of type $(H\text{-}S)/F$ was calculated following Gaussian propagation of uncertainty, as illustrated here in equation 3.2.5 for the error of CHR_1:

$$\begin{aligned} ECHR_1 = \Bigg[& \left(\left(-\frac{1}{F} - (B_2 - B_1) \cdot \frac{1}{F^2} \right) \cdot EB_1 \right)^2 + \\ & + \left(\left(\frac{1}{F} - (B_2 - B_1) \cdot \frac{1}{F^2} \right) \cdot EB_2 \right)^2 + \\ & + \left(-(B_2 - B_1) \cdot \frac{1}{F^2} \cdot EB_3 \right)^2 + \\ & + \left(-(B_2 - B_1) \cdot \frac{1}{F^2} \cdot EB_4 \right)^2 \Bigg]^{1/2} \end{aligned} \tag{3.2.5}$$

3.3. Cross-matching with Catalogs at Other Wavelengths

At this point in the analysis, the sources were cross-matched against catalogs at other wavelengths.
Cross-matching is a very important tool for population studies, as many objects exhibit a variety of different features across the electromagnetic spectrum. Thus, the properties of counterparts at other wavelengths often play a key role in the identification of the object.

For cross-matching of the sources with catalogs of different wavelengths, a version of the NWAY algorithm by Salvato et al. (2018) was used. This version was written by Jonathan Knies (Dr. Karl Remeis-Observatory Bamberg). The sources were cross-matched against the infrared catalogs allWISE (Cutri et al., 2014), 2mass (Skrutskie et al., 2006), and the optical SkyMapper catalog (Wolf et al., 2018) using the NWAY algorithm. For cross-correlation with the optical USNO-B1.0 catalog (Monet et al., 2003) as well as the radio catalogs SPECFINDV (Vollmer, B. et al., 2010) and the Sydney University Molonglo Sky Survey (SUMSS V2.1) (Mauch et al., 2003) the CDS X-Matching online tool (`http://cdsxmatch.u-strasbg.fr/`) was used. The sources could not be cross-correlated against the SDSS (Sloan Digital Sky Survey) catalog, as it does not cover this part of the southern hemisphere.

In the following analysis the allWISE bands W1, W2, and W3 were used, as were the 2mass bands J and K. Furthermore USNO-B bands B2, R2, and I were used, as well as Skymapper bands g, r, and i.

Duplicates in this correlation, where two X-ray sources were matched to a single optical or infrared source, were found through the use of a python script (written by me). The script checked the distance between the X-ray coordinates and the coordinates of the optical or infrared source and eliminated the match that was further away.

3.4. Interpreting the Diagrams

Using the Chandra counts, the calculated hardness ratios, and the information gained through cross-matching, a number of plots were produced, that allow some conclusions as to the nature of the X-ray sources found in Cen A. These conclusions will now be presented, sorted by the type of object they concern. Afterwards the hardness ratios will be addressed specifically.

3.4.1. Foreground Stars

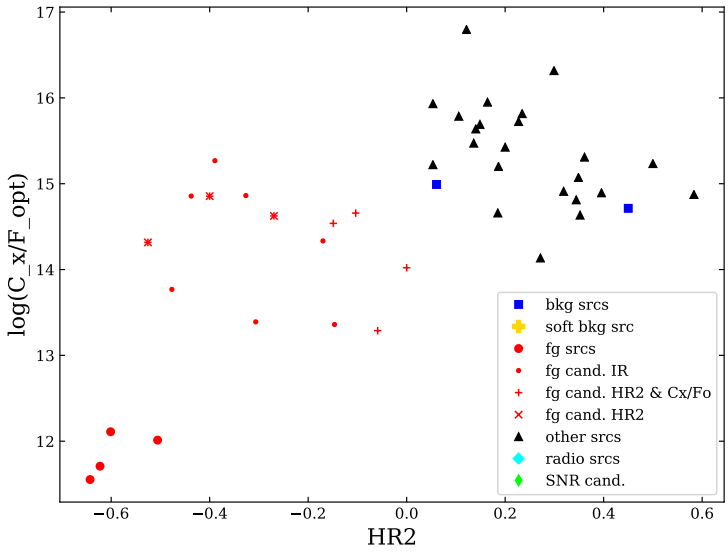

Figure 3.4.: $\log(C_x/F_{opt})$ against HR2

The diagram shown in Figure 3.4 allows us to identify four foreground stars. For this diagram the value of $\log\left(\frac{C_x}{F_{opt}}\right)$ was calculated according to Saeedi et al. (2019) using a

version of the equation by Maccacaro et al. (1988) that was modified by Saeedi et al. (2016) as follows:

$$\log\left(\frac{C_x}{F_{opt}}\right) = \log_{10}(C_x) + \frac{\mathrm{B2} + \mathrm{R2}}{2 \times 2.5} + 5.37 \tag{3.4.1}$$

Instead of g, r, and the flux F_x that were used by Saeedi et al. (2019), the USNO-B magnitudes B2 and R2 as well as the X-ray counts C_x over all bands were used. Thus, the calculated values may not correspond exactly to the $\log\left(\frac{F_x}{F_{opt}}\right)$ that was calculated by Saeedi et al. (2019), but can still be compared against one another.

By plotting these values against HR_2, four foreground stars could be identified. They can be seen in Figure 3.4, as they stand out through their low HR_2 and their low $\frac{C_x}{F_{opt}}$. All the sources with $HR_2 < 0.01$ in this plot, that had not already been labeled as foreground star candidates through other plots, were labeled as such, as can be seen in the plot labels.

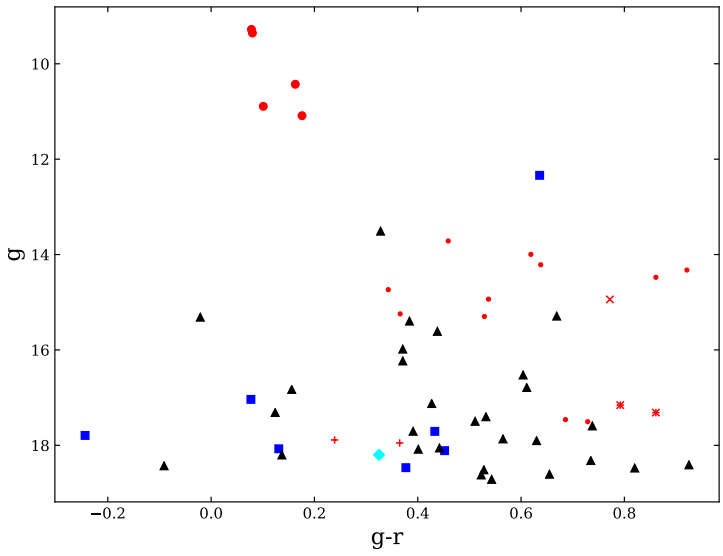

Figure 3.5.: Color-magnitude diagram of Skymapper magnitudes

A fifth foreground star could be identified through its position in the optical color-magnitude diagram that can be seen in Figure 3.5.

Further foreground star candidates could be identified through the infrared color-color diagram in Figure 3.6. The objects with $\mathrm{W2} - \mathrm{W3} < 0.5$, that are clustered around the foreground sources, are considered foreground candidates as well.

A final group of foreground candidates was found through the HR-diagram in Figure 3.7. All non-background sources with $HR_2 < -0.2$ were also classified as foreground star candidates due to the softness of their spectrum. It can be noted that the five foreground stars can also be found in the same area of Figure 3.7.

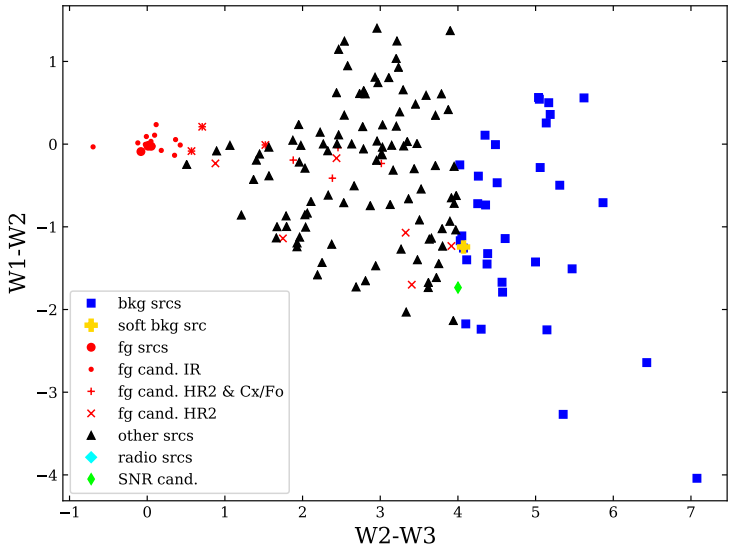

Figure 3.6.: Color-color diagram of allWISE magnitudes

3.4.2. Background Sources

Cross-correlation with quasar catalogs did not yield significant matches, so for the identification of background sources the allWISE infrared magnitudes were chosen instead.

The criterion chosen to separate background sources from the other sources is visible in Figure 3.6. First the background sources were separated in accordance with Saeedi et al. (2019). As the galaxy analyzed in that paper is, however, very different from Cen A, after some consultation all sources with $W2 - W3 > 4$ were denoted as background sources, i.e. galaxies and AGNs, in accordance with Salvato et al. (2018).

One, in terms of hardness ratios, very soft background source was also specifically isolated to track its position on further diagrams.

3.4.3. SNRs

Another interesting discovery made in Figure 3.7 are the two radio sources with a soft X-ray emission. These were hereafter denoted as SNR candidates.

3.4.4. Hardness Ratio Diagrams

Both sets of hardness ratios were plotted against one another, as can be seen in the following figures.

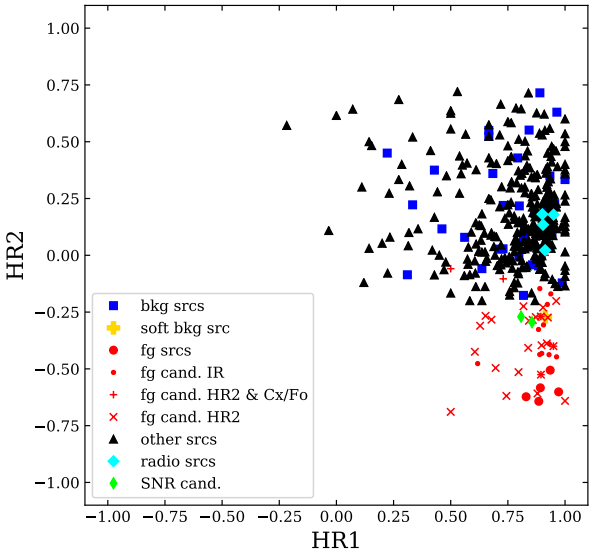

Figure 3.7.: HR_1-HR_2 diagram

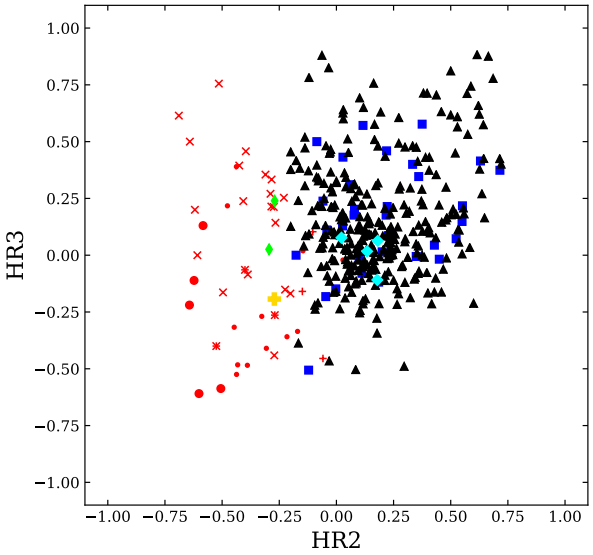

Figure 3.8.: HR_2-HR_3 diagram

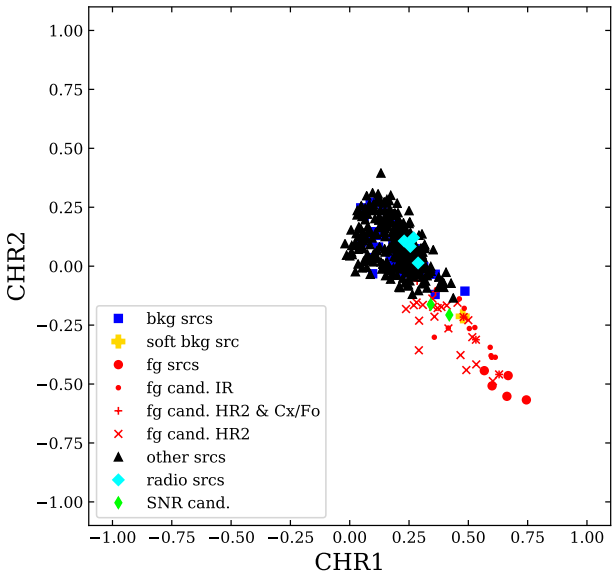

Figure 3.9.: CHR_1-CHR_2 diagram

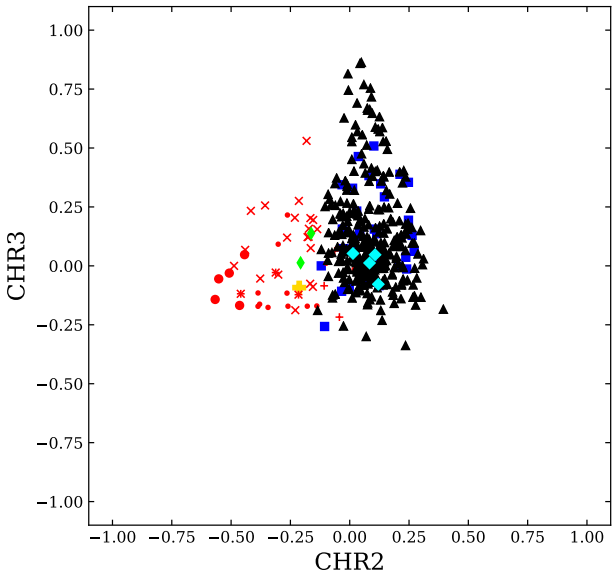

Figure 3.10.: CHR_2-CHR_3 diagram

As $HR_2 < -0.2$ was used as a criterion for finding foreground star candidates, the observation that all foreground star candidates in Figure 3.7 and 3.8 (even those found through other criteria) possess a value of $HR_2 < 0$ may hold little weight. It does, however, become clear in Figure 3.7 that all foreground stars and candidates fulfill $HR_1 > 0.5$, which points to a strong emission in the soft band. This fits the expectations for foreground sources.

HR_3 does not make a distinction between different types of sources possible, which is interesting, as some foreground star candidates show quite high HR_3 values. This might, however, be explained by looking at the equation used to calculate these hardness ratios (eq. 3.2.2). Should a source have a low number of counts in the medium as well as in the hard band, even small differences in these values could cause high fluctuations in the values of HR_3.

The CHR diagrams shown in Figure 3.9 and 3.10 paint a similar picture. However, the CHR values are generally smaller, while the differences in their distributions are more extreme. This can be explained by the different equation (eq. 3.2.4) used to obtain these values, which does not only divide (H-S) through the sum of the counts of those two bands, but through the total counts. This highlights differences in hardness ratios even more.

This effect can be seen in Figure 3.9, where the CHR_1 values of the foreground sources diverge even stronger from those of the background and of the unidentified sources. The effect is also visible in Figure 3.10, where the unidentified sources with high CHR_3 values stand out against the rest.

Generally, it can be said that the hardness ratio diagrams show a difference in the behavior of foreground and background sources. Meanwhile, the as of yet unidentified sources and background sources are found in the same general area of the diagrams, which is to be expected.

3.4.5. Other Plots

A number of other plots, that were made in the course of this analysis, did not lead to concrete conclusions as to the nature of certain X-ray sources. However, tendencies in their distribution could still be observed.

Figure 3.11, for instance, shows a color-magnitude diagram in the infrared. It can be observed that the foreground stars group together at the top of the frame due to their low infrared magnitudes. It can also be seen that all foreground stars and candidates have similar J−K colors of approximately $0 - 2$.

The rest of the plots can be found in the appendix A.2, starting on p. 32.

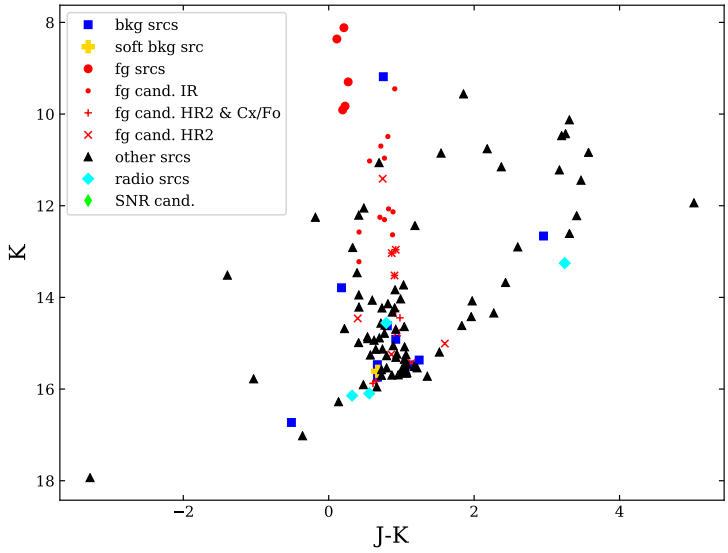

Figure 3.11.: 2mass color-magnitude diagrams

3.5. Isochrones

Lastly, an optical color-magnitude diagram was examined using isochrones.
Isochrones are theoretically calculates curves, indicating the placement of stellar populations of a certain age and metallicity in a color-magnitude diagram. Thus, conclusions as to the age and metallicities (and, depending on the respective model, other factors) of the stellar population of the region in question can be drawn.

In this thesis isochrones were used to take a look at different star populations in the observed sources in the field of view of Cen A. Several isochrones were plotted into an optical color-magnitude diagram of their USNO-B counterparts to indicate the location of different populations of certain respective ages and metallicities.

For this purpose theoretical isochrones by Girardi et al. (2004) were used. As the bands of the USNO-B catalog are largely incompatible with the bands of many catalogs, the theoretical isochrones calculated for the SDSS (Sloan Digital Sky Survey) bands were chosen.

To compare the theoretical isochrones with the USNO-B magnitudes, the SDSS magnitudes had to be converted, which was accomplished using the conversation formula for the second

epoch magnitudes of USNO-B by Monet et al. (2003):

$$B2 = g' + 0.079 \cdot (g' - r') + 0.06 \tag{3.5.1}$$
$$R2 = r' - 0.109 \cdot (g' - r') - 0.09 \tag{3.5.2}$$
$$I = i' - 0.164 \cdot (r' - i') - 0.44 \tag{3.5.3}$$

The identification of the different identifiers used for the USNO-B bands was made possible through the publication by Madsen and Gaensler (2013).

Different isochrones for different metallicities and ages were plotted into the optical color-magnitude diagram. One of them represents the central region of Cen A in accordance with the youngest population with the highest metallicity considered by Karataeva et al. (2006) ($\log_{10}(\text{age}) = 6.95$, $Z = 0.019$). To describe the halo, isochrones were plotted in accordance with the extremes in terms of age and metallicity (highest metallicity, lowest age and lowest metallicity, highest age) found by Rejkuba et al. (2011), which amounted to ($\log_{10}(\text{age}) = 9.3$, $Z = 0.030$) and ($\log_{10}(\text{age}) = 10.05$, $Z = 0.0001$) respectively. The youngest iteration of the theoretical isochrone for the maximum metallicity observed in the halo was plotted as well ($\log_{10}(\text{age}) = 7.8$, $Z = 0.030$).

All of the isochrones for Cen A were corrected via the distance module for the distance of $d = 3.8\,\text{Mpc}$ (Harris et al., 2010) as follows:

$$m = M + 5\log_{10}(d) - 5 \tag{3.5.4}$$

The isochrones for Cen A were also corrected for galactic extinction A in each respective band using the NASA/IPAC EXTRAGALACTIC DATABASE search (`https://ned.ipac.caltech.edu/forms/byname.html`) as follows:

$$m_{\text{corrected}} = m + A \tag{3.5.5}$$

The NASA/IPAC EXTRAGALACTIC DATABASE extinction values for Cen A in the SDSS bands can be found in Table 3.4.

Three isochrones were also plotted to describe the foreground star population. Considering the sun to be a typical main sequence star with a metallicity of $Z_\odot = 0.0196 \pm 0.0014$ according to Vagnozzi (2019), a metallicity of $Z = 0.019$ was chosen. Furthermore an age of $\log_{10} = 9.65$ was used, which corresponds to the solar age according to Bonanno et al. (2002). The isochrones were plotted using the distance module (eq. 3.5.4) for distances of $d = 10\,\text{pc}$, $d = 100\,\text{pc}$, and $d = 200\,\text{pc}$ to account for the extent of the Milky Way. They were not corrected for galactic extinction, as they describe objects within the Milky Way.

SDSS band	galactic extinction [mag]
u'	0.487
g'	0.379
r'	0.262
i'	0.195
z'	0.145

Table 3.4.: SDSS galactic extinction values

Considering the position of the isochrones and the optical counterparts in the diagram shown in Figure 3.12, some conclusions can be drawn. The foreground stars are close to the foreground isochrones for $d = 100\,\mathrm{pc}$ and $d = 200\,\mathrm{pc}$, suggesting that the foreground stars may be found at distances of this order of magnitude.

The isochrones describing Cen A, however, draw a different picture. It becomes clear that the isochrones describing the halo do not seem to coincide with the optical counterparts at all; they are a lot less bright. Only the isochrone describing the very youngest stellar population of the central part of Cen A ($\log_{10}(\mathrm{age}) = 6.95$, $Z = 0.019$) coincides with the optical counterparts at all. This leads to the conclusion that only the very brightest sources of Cen A possess an optical counterpart that is listed in the USNO-B catalog. Objects with $B2 \gtrsim 20$ are, presumably, simply too far away and/or too faint to be detected. This may, in part, also be due to the slight datedness of the USNO-B catalog and due to the nature of the as of yet unidentified sources.

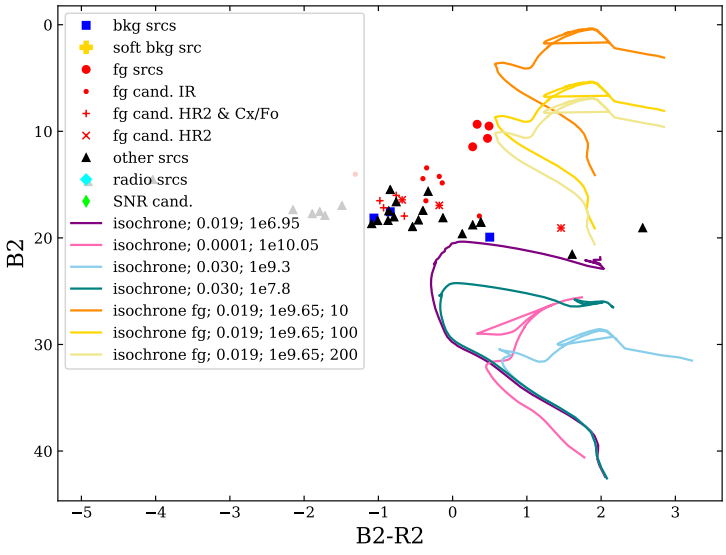

Figure 3.12.: USNO-B color-magnitude diagram with isochrones

4. Conclusion and Outlook

In the course of this bachelor's thesis Chandra data of the galaxy Centaurus A taken over almost twenty years were analyzed.

After an introduction into the characteristics of Cen A, information on the Chandra X-ray Observatory, and some insight into the sources relevant in this work, the analysis was undertaken.

Excluding the jet, 418 X-ray point sources could be found. Through the use of all available data, be it the extracted counts, calculated hardness ratios, or counterparts found through cross-matching, a lot of insight into the nature of Cen A's X-ray population was achieved. Five foreground stars could be identified by the low ratio of their X-ray counts to their optical magnitudes and their optical counterparts. Foreground star candidates were found through the aforementioned ratio as well as through study of their hardness ratios and infrared counterparts. Background candidates were identified by their infrared counterparts. Two sources could also be identified as SNR candidates through their soft X-ray counts and the existence of a radio counterpart.

Isochrones were plotted into an optical color-magnitude diagram to study different stellar populations. A correlation of the isochrones with the foreground stars and a few, optically rather bright, sources of Cen A could be observed. Many sources, however, seem to be too far away to be detected.

So far, the X-ray sources detected by Chandra could be sorted to a certain degree, however, the nature of many sources still remains unclear. To that effect, the temporal variability and the spectra of the, as of yet, unidentified sources will be analyzed in the future and hopefully provide further insight. Further cross-correlation with galaxy, quasar, and SNR catalogs will hopefully confirm some of the candidates found in this analysis.

Acknowledgments

The analysis described in this thesis is the result not only of work done by me, but was made possible through collaboration with others. In this concluding section, I would like to list every person that was part of this analysis as well as their contributions to make clear which part of the work is to be be attributed to which person.

The Chandra data were reprocessed by me. Afterwards the destreaking, stacking, source detection, and extraction of the source regions were conducted by Tathagata Saha and Alex Markowitz from the Nicolaus Copernicus Astronomical Center in Warsaw.
I then manually sorted through the sources in order to identify valid X-ray sources. I also added some sources, that had been missed in the detection process.

The individual regions and spectra of all valid X-ray sources, that are not part of the jet, were then extracted by Prof. Dr. Jörn Wilms (Dr. Karl Remeis-Observatory Bamberg).
Using these spectra, I wrote and applied the isis script that extracted counts for the sources and used these to calculate hardness ratios.
This research has made use of ISIS functions (ISISscripts) provided by ECAP/Remeis observatory and MIT (http://www.sternwarte.uni-erlangen.de/isis/).

A variation of the NWAY algorithm was written by Jonathan Knies (Dr. Karl Remeis-Observatory Bamberg). I used this variation, as well as the X-matching online tool, to cross-correlate the X-ray sources against catalogs at other wavelengths.

The rest of the analysis, sorting through, and plotting of the results was done by me, under the supervision of Prof. Dr. Manami Sasaki (Dr. Karl Remeis-Observatory Bamberg), my thesis advisor.

Bibliography

Bolton, J. G. (1948). Discrete Sources of Galactic Radio Frequency Noise. *Nature*, 162(4108):141–142.

Bolton, J. G., Stanley, G. J., and Slee, O. B. (1949). Positions of Three Discrete Sources of Galactic Radio-Frequency Radiation. *Nature*, 164(4159):101–102.

Bonanno, A., Schlattl, H., and Paternò, L. (2002). The age of the Sun and the relativistic corrections in the EOS. *Astronomy & Astrophysics*, 390:1115–1118.

Bowyer, C. S., Lampton, M., Mack, J., and de Mendonca, F. (1970). Detection of X-Ray Emission from 3c 273 and NGC 5128. *Astrophysical Journal*, 161:L1.

Brissenden, R. J. (2001). Chandra X-ray Observatory Operations. In Harnden, F., Primini, F. A., and Payne, H. E., editors, *Astronomical Data Analysis Software and Systems X*, volume 238 of *Astronomical Society of the Pacific Conference Series*, page 22.

Chandra X-Ray Observatory (2009a). ACIS Instrument Information. https://cxc.harvard.edu/cal/Acis/index.html, last accessed on 08 May 2020.

Chandra X-Ray Observatory (2009b). HRC Instrument Information. https://cxc.harvard.edu/cal/Hrc/index.html, last accessed on 08 May 2020.

Chandra X-Ray Observatory (2009c). Telescope System: Telescope Schematic Illustrations. https://chandra.harvard.edu/resources/illustrations/teleSchem.html#xray_mirror, last accessed on 13 March 2020.

Chandra X-Ray Observatory (2019). Energy bands. https://cxc.harvard.edu/csc/columns/ebands.html, last accessed on 20 February 2020.

Cutri, R. M., Wright, E. L., Conrow, T., Fowler, J. W., Eisenhardt, P. R. M., Grillmair, C., Kirkpatrick, J. D., Masci, F., McCallon, H. L., Wheelock, S. L., Fajardo-Acosta, S., Yan, L., Benford, D., Harbut, M., Jarrett, T., Lake, S., Leisawitz, D., Ressler, M. E., Stanford, S. A., Tsai, C. W., Liu, F., Helou, G., Mainzer, A., Gettings, D., Gonzalez, A., Hoffman, D., Marsh, K. A., Padgett, D., Skrutskie, M. F., Beck, R. P., Papin, M., and Wittman, M. (2014). Explanatory Supplement to the AllWISE Data Release Products. http://wise2.ipac.caltech.edu/docs/release/allwise/expsup/, last accessed on 21 May 2020.

Fabbiano, G. (2006). Populations of X-Ray Sources in Galaxies. *Annual Review of Astronomy and Astrophysics*, 44(1):323–366.

Fanaroff, B. L. and Riley, J. M. (1974). The morphology of extragalactic radio sources of high and low luminosity. *Monthly Notices of the Royal Astronomical Society*, 167:31P–36P.

Garmire, G. P., Bautz, M. W., Ford, P. G., Nousek, J. A., and Ricker, George R., J. (2003). Advanced CCD imaging spectrometer (ACIS) instrument on the Chandra X-ray Observatory. In Truemper, J. E. and Tananbaum, H. D., editors, *X-Ray and Gamma-Ray Telescopes and Instruments for Astronomy*, volume 4851 of *Society of Photo-Optical Instrumentation Engineers (SPIE) Conference Series*, pages 28–44. SPIE.

Girardi, L., Grebel, E., Odenkirchen, M., and Chiosi, C. (2004). Theoretical isochrones in several photometric systems - II. The Sloan Digital Sky Survey ugriz system. *Astronomy & Astrophysics*, 422(1):205–215.

Harris, G. L. H., Rejkuba, M., and Harris, W. E. (2010). The Distance to NGC 5128 (Centaurus A). *Publications of the Astronomical Society of Australia*, 27(4):457–462.

HEASARC (2012). HEASARC Picture of the week. Credit: X-ray: NASA/CXC/CfA/R.Kraft et al; Radio: NSF/VLA/Univ.Hertfordshire/M.Hardcastle; Optical: ESO/VLT/ISAAC/M.Rejkuba et al. https://heasarc.gsfc.nasa.gov/docs/objects/heapow/archive/active_galaxies/cena_composite.html, last accessed on 08 May 2020.

Israel, F. P. (1998). Centaurus A - NGC 5128. *Astronomy and Astrophysics Review*, 8(4):237–278.

Karataeva, G. M., Tikhonov, N. A., Galazutdinova, O. A., and Hagen-Thorn, V. A. (2006). Stellar population of the central regions of NGC 5128. *Astronomy Letters*, 32(4):236–243.

Maccacaro, T., Gioia, I. M., Wolter, A., Zamorani, G., and Stocke, J. T. (1988). The X-Ray Spectra of the Extragalactic Sources in the Einstein Extended Medium-Sensitivity Survey. *The Astrophysical Journal*, 326:680.

Madsen, G. J. and Gaensler, B. M. (2013). A Precision Multi-band Two-epoch Photometric Catalog of 44 Million Sources in the Northern Sky from a Combination of the USNO-B and Sloan Digital Sky Survey Catalogs. *The Astrophysical Journal Supplement Series*, 209(2):33.

Mauch, T., Murphy, T., Buttery, H. J., Curran, J., Hunstead, R. W., Piestrzynski, B., Robertson, J. G., and Sadler, E. M. (2003). SUMSS: a wide-field radio imaging survey of the southern sky – II. The source catalogue. *Monthly Notices of the Royal Astronomical Society*, 342(4):1117–1130.

McKinley, B., Tingay, S. J., Carretti, E., Ellis, S., Bland-Hawthorn, J., Morganti, R., Line, J., McDonald, M., Veilleux, S., Wahl Olsen, R., Sidonio, M., Ekers, R., Offringa, A. R., Procopio, P., Pindor, B., Wayth, R. B., Hurley-Walker, N., Bernardi, G., Gaensler,

B. M., Haverkorn, M., Kesteven, M., Poppi, S., and Staveley-Smith, L. (2018). The jet/wind outflow in Centaurus A: a local laboratory for AGN feedback. *Monthly Notices of the Royal Astronomical Society*, 474(3):4056–4072.

Merritt, D. and Ferrarese, L. (2001). The $M_\bullet$-σ Relation for Supermassive Black Holes. *The Astrophysical Journal*, 547(1):140–145.

Monet, D. G., Levine, S. E., Canzian, B., Ables, H. D., Bird, A. R., Dahn, C. C., Guetter, H. H., Harris, H. C., Henden, A. A., Leggett, S. K., and et al. (2003). The USNO-B Catalog. *The Astronomical Journal*, 125(2):984–993.

Neumayer, N. (2010). The Supermassive Black Hole at the Heart of Centaurus A: Revealed by the Kinematics of Gas and Stars. *Publications of the Astronomical Society of Australia*, 27(4):449–456.

Pietsch, W. (2008). X-ray source population studies in nearby galaxies. *Mem. Societa Astronomica Italiana*, 79:198.

Rejkuba, M., Harris, W., Greggio, L., and Harris, G. (2011). How old are the stars in the halo of NGC8 (Centaurus A)? . *Astronomy & Astrophysics*, 526:A123.

Saeedi, S., Sasaki, M., and Ducci, L. (2016). XMM-Newton study of the Draco dwarf spheroidal galaxy. *Astronomy & Astrophysics*, 586:A64.

Saeedi, S., Sasaki, M., Stelzer, B., and Ducci, L. (2019). Classification of low-luminosity stellar X-ray sources in the field of the Draco dwarf spheroidal galaxy. *Astronomy & Astrophysics*, 627:19 pp.

Salvato, M., Buchner, J., Budavári, T., Dwelly, T., Merloni, A., Brusa, M., Rau, A., Fotopoulou, S., and Nand ra, K. (2018). Finding counterparts for all-sky X-ray surveys with NWAY: a Bayesian algorithm for cross-matching multiple catalogues. *Monthly Notices of the Royal Astronomical Society*, 473(4):4937–4955.

Sasaki, M., Haberl, F., Henze, M., Saeedi, S., Williams, B., Plucinsky, P., Hatzidimitriou, D., Karampelas, A., Sokolovsky, K., Breitschwerdt, D., de Avillez, M., Filipovi´c, M., Galvin, T., Kavanagh, P., and Long, K. (2018). Deep XMM-Newton observations of the northern disc of M 31 - I. Source catalogue. *Astronomy & Astrophysics*, 620:A28.

Schwartz, D. A. (2011). Optics. In Arnaud, K., Smith, R., and Siemiginowska, A., editors, *Handbook of X-ray Astronomy*, Cambridge Observing Handbooks for Research Astronomers, page 6–22. Cambridge University Press.

Seward, F. D. and Charles, P. A. (2010). *Exploring the X-ray Universe*. Cambridge University Press, 2 edition.

Skrutskie, M. F., Cutri, R. M., Stiening, R., Weinberg, M. D., Schneider, S., Carpenter, J. M., Beichman, C., Capps, R., Chester, T., Elias, J., Huchra, J., Liebert, J., Lonsdale, C., Monet, D. G., Price, S., Seitzer, P., Jarrett, T., Kirkpatrick, J. D., Gizis, J. E., Howard, E., Evans, T., Fowler, J., Fullmer, L., Hurt, R., Light, R., Kopan, E. L., Marsh, K. A., McCallon, H. L., Tam, R., Van Dyk, S., and Wheelock, S. (2006). The Two Micron All Sky Survey (2MASS). *The Astronomical Journal*, 131(2):1163–1183.

Vagnozzi, S. (2019). New solar metallicity measurements. *Atoms*, 7(2):41.

Vollmer, B., Gassmann, B., Derrière, S., Boch, T., Louys, M., Bonnarel, F., Dubois, P., Genova, F., and Ochsenbein, F. (2010). The SPECFIND V2.0 catalogue of radio cross-identifications and spectra - SPECFIND meets the Virtual Observatory. *Astronomy & Astrophysics*, 511:A53.

Voss, R. and Gilfanov, M. (2006). The luminosity function of X-ray point sources in Centaurus A. *Astronomy & Astrophysics*, 447(1):71–80.

Wolf, C., Onken, C. A., Luvaul, L. C., Schmidt, B. P., Bessell, M. S., Chang, S.-W., Da Costa, G. S., Mackey, D., Martin-Jones, T., Murphy, S. J., Preston, T., Scalzo, R. A., Shao, L., Smillie, J., Tisserand, P., White, M. C., and Yuan, F. (2018). SkyMapper Southern Survey: First Data Release (DR1). *Publications of the Astronomical Society of Australia*, 35:e010.

Woodley, K. A., Raychaudhury, S., Kraft, R. P., Harris, W. E., Jordán, A., Whitaker, K. E., Jones, C., Forman, W. R., and Murray, S. S. (2008). Globular Clusters and X-Ray Point Sources in Centaurus A (NGC 5128). *The Astrophysical Journal*, 682(1):199–211.

A. Appendix

A.1. Observation IDs of the Analyzed Data

316, 962, 1600, 1601, 2978, 3965, 7797, 7798, 7799, 7800, 8489, 8490, 10722, 10723, 10724, 10725, 10726, 11846, 11847, 12155, 12156, 13303, 13304, 15294, 15295, 16276, 16277, 17471, 17472, 17890, 17891, 18461, 18462, 19521, 19747, 19748, 20585, 20752, 20794, 22189

A.2. Plots

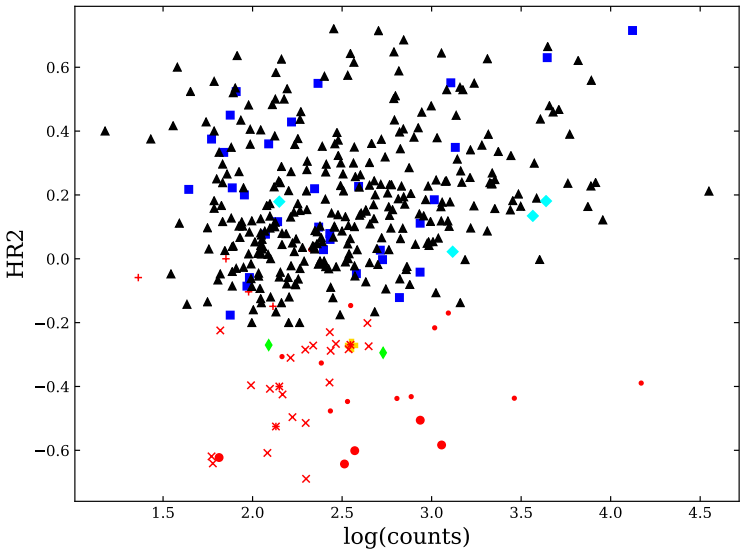

Figure A.1.: log(counts)/HR2 diagram

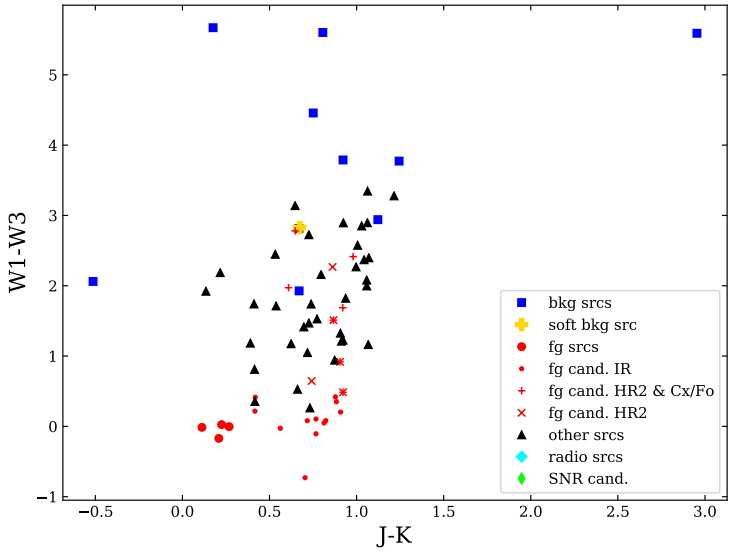

Figure A.2.: 2mass/allWISE color-color diagram

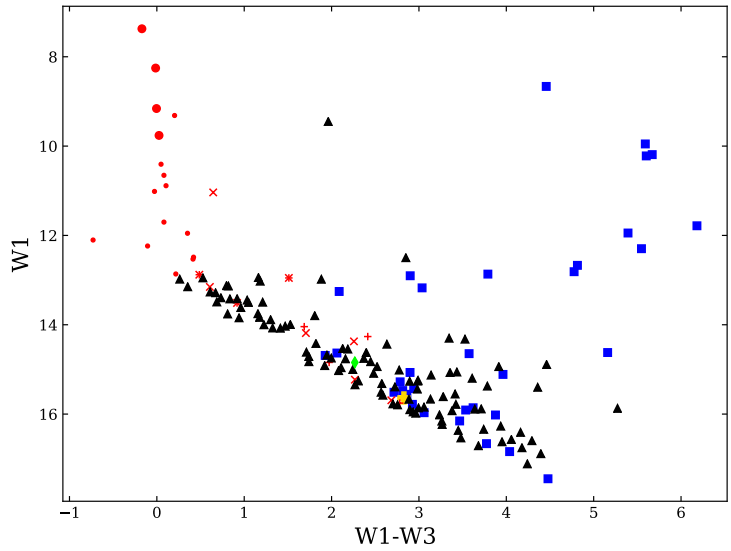

Figure A.3.: allWISE color-magnitude diagram

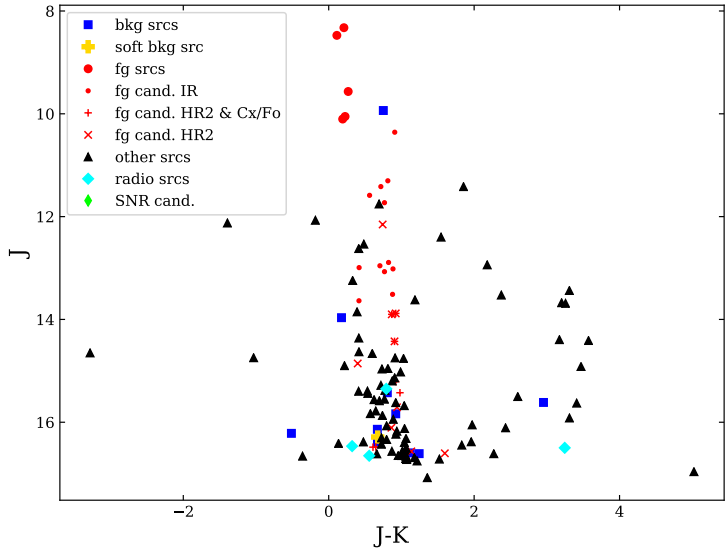

Figure A.4.: 2mass color-magnitude diagram

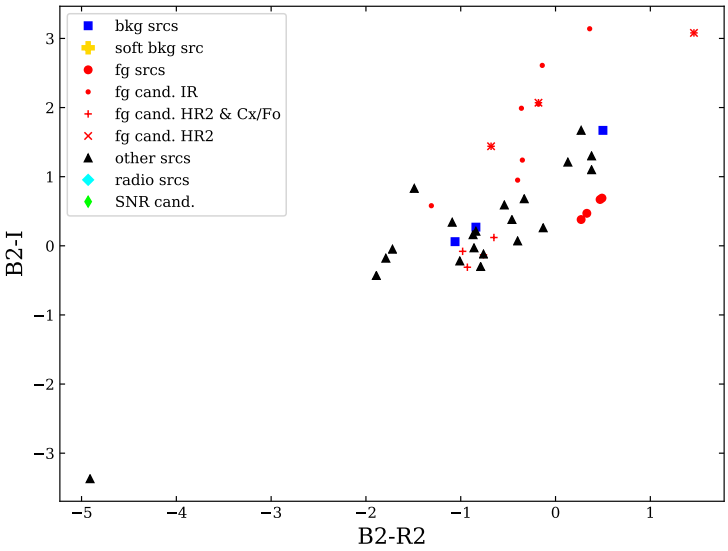

Figure A.5.: USNO-B color-color diagram

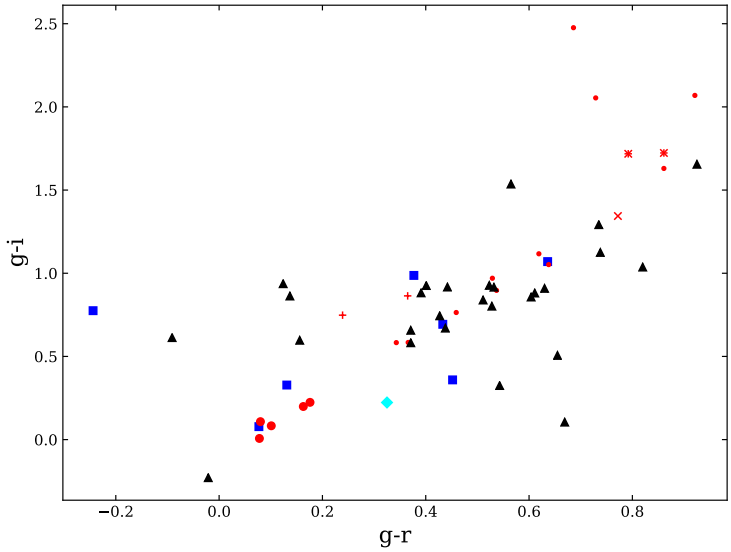

Figure A.6.: Skymapper color-color diagram

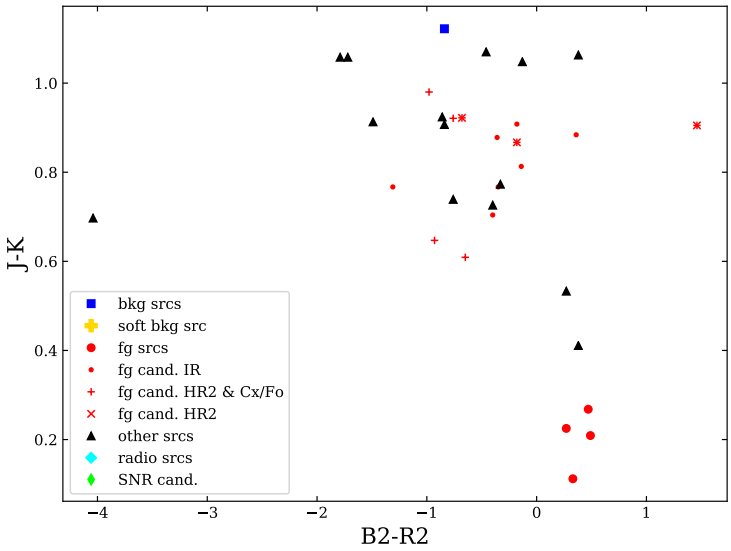

Figure A.7.: USNO-B/2mass color-color diagram

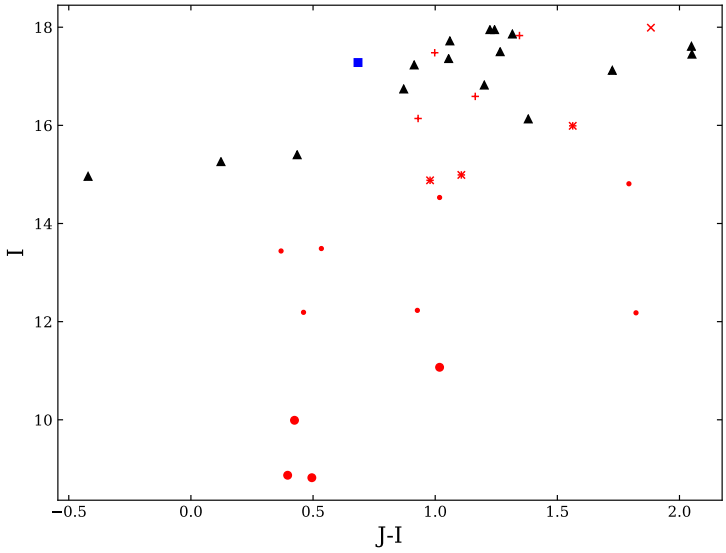

Figure A.8.: USNO-B/2mass color-magnitude diagram

Erklärung:

Hiermit bestätige ich, dass ich diese Arbeit selbständig und nur unter Verwendung der angegebenen Hilfsmittel angefertigt habe.